Materials Today Energy 31 (2023) 101224

Contents lists available at ScienceDirect

Materials Today Energy

journal homepage: www.journals.elsevier.com/materials-today-energy/

Correlative full field X-ray compton scattering imaging and X-ray computed tomography for *in situ* observation of Li ion batteries

Chu Lun Alex Leung [a, b], Matthew D. Wilson [c], Thomas Connolley [d], Stephen P. Collins [d], Oxana V. Magdysyuk [d], Matthieu N. Boone [e], Kosuke Suzuki [f], Matthew C. Veale [a], Enzo Liotti [g], Frederic Van Assche [e], Andrew Lui [g], Chun Huang [b, h, i, *, 1]

[a] Department of Mechanical Engineering, University College London, London, WC1E 7JE, UK
[b] Research Complex at Harwell, Rutherford Appleton Laboratory, Didcot, Oxfordshire, OX11 0FA, UK
[c] STFC-UKRI, Rutherford Appleton Laboratory, Harwell Campus, Didcot, Oxfordshire, OX11 0QX, UK
[d] Diamond Light Source, Harwell Campus, Didcot, Oxfordshire, OX11 0QX, UK
[e] Radiation Physics, Dept. Physics and Astronomy, Faculty of Sciences, Ghent University; Proeftuinstraat 86/N12, 9000 Gent, Belgium
[f] Faculty of Science and Technology, Gunma University, 1-5-1 Tenjin-cho, Kiryu, Gunma 376-8515, Japan
[g] Department of Materials, University of Oxford, Oxford, OX1 3PH, UK
[h] Department of Materials, Imperial College London, London, SW7 2AZ, UK
[i] The Faraday Institution, Quad One, Becquerel Ave, Harwell Campus, Didcot, OX11 0RA, UK

ARTICLE INFO

Article history:
Received 4 August 2022
Received in revised form
12 November 2022
Accepted 2 December 2022
Available online 6 December 2022

Keywords:
Electrode design
Thick electrodes
Directional ice templating
Correlative imaging
X-ray compton scattering

ABSTRACT

Increasing electrode thickness is gaining more attention as a potential route to increase energy density for Li ion batteries although the realizable capacity and rate capability are usually limited by Li^+ ion diffusion during (dis)charge, especially at increased (dis)charge rates. It remains challenging to visualize and quantify the low atomic number Li^+ chemical stoichiometry distribution inside the electrode within commercially standard battery geometry, e.g. coin cells with stainless steel casings. Here, we map the distribution of Li^+ chemical stoichiometry in the electrode microstructure inside a working coin cell battery to show the amount of electrode materials contributing to energy storage performance using innovative *in situ* correlative full-field X-ray Compton scattering imaging (XCS-I) and X-ray computed tomography (XCT). We design and fabricate an ultra-thick (~1 mm) cathode of $LiNi_{0.8}Mn_{0.1}Co_{0.1}O_2$ with a microstructure containing vertically oriented pore arrays using a directional ice templating method. This novel technique paves a new way to map low atomic number elements in 3D structures and study how the microstructure improves Li^+ ion diffusivity and energy storage performance.

1. Introduction

Batteries are one of the key technologies in the net zero transition, e.g. in zero-emission electric transportation and for electricity storage from intermittent renewable sources such as solar and wind [1–3]. Li^+ ion batteries (LIBs) are currently one of the most widely used types of batteries [4–7]. Most LIB electrodes are thin (50–100 μm [8,9]) and made by scalable slurry coating (SC) [10,11]. The electrode microstructure usually contains highly tortuous pores that restrict Li^+ ion diffusion [12,13]. Increasing electrode thickness is a promising method to reduce the proportion of inactive components such as metallic current collectors (Cu and Al foils) and separators in the battery cell-stacks and to increase energy density [4]. However, Li^+ ion diffusion is further impeded in the thick electrodes with the tortuous porous microstructure, and the capacity and rate capability of these batteries are reduced to an impractical level [14–17]. Different processing methods have made bespoke electrode microstructure to improve energy storage performance, e.g. co-extrusion [18], magnetic templating [19], infiltration of natural wood framework [20]. We have previously developed a directional ice templating (DIT) technique that can fabricate thick (~1 mm) electrodes of $LiCoO_2$ and $LiFePO_4$ containing vertically oriented pore arrays to improve Li^+ ion diffusion [21–23]. However, the connection between Li^+ ion diffusion in the microstructure and the amount of energy storage in the electrode active material is still elusive.

* Corresponding author.
E-mail address: a.huang@imperial.ac.uk (C. Huang).
[1] Dr Chun Huang's first affiliation is h Department of Materials, Imperial College London, London, SW7 2AZ, UK.

https://doi.org/10.1016/j.mtener.2022.101224

Various *in situ* synchrotron X-ray characterization techniques have been used to study energy storage materials. X-ray computed tomography (XCT) has been used to image electrode microstructure in 3D, though it cannot provide detailed information related to its chemical constituents [24]. X-ray diffraction (XRD) studies the crystal structure and lattice spacing of the electrode materials [25]. Bragg scattering and diffuse scattering coupled with pair distribution function (PDF) analysis study the regular and irregular arrangement of atoms on the lattice sites [26]. X-ray absorption spectroscopy (XAS) and transmission X-ray microscopy (TXM) coupled with X-ray near-edge absorption spectroscopy (XANES) show the change of oxidation state of elements in electrode active materials, mainly heavy transition metal (TM) elements [27,28]. However, it remains challenging to directly visualize and quantify the chemical stoichiometry distribution of low atomic mass ions such as Li^+ using abovementioned techniques because there are fewer electron orbitals in a Li atom compared with other elements, it is less likely to generate characteristic X-rays compared with heavy elements [29]. Other types of characterization techniques such as nuclear magnetic resonance (NMR) [30,31] and neutron diffraction [17] are among the few techniques that can detect Li but also have their complications, e.g. restrictions on the configuration of the *in situ* testing cells [32] and brightness of the source [33].

X-ray Compton scattering (XCS) measures the energy of the incoherently scattered photons from the object [34–36]. Although XCS has not been widely used compared with the abovementioned techniques, it is unique for detecting the interaction between incident photons and valence electrons which are involved in the Li^+ intercalation and extraction redox reactions. Current challenges are as follows: (i) previous XCS studies used an X-ray pencil beam to perform raster scanning of the battery sample and used a collimated Ge solid-state detector (Ge-SSD) to measure the intensity of the incoherent scattered X-rays. This pencil beam XCS imaging is time consuming (~30 h for scanning the cathode size of a coin cell battery [37,38]), resulting in restricted scanning volume; (ii) to date, different properties (e.g. chemical composition, physical microstructural changes, etc.) of the battery samples are usually investigated separately by different techniques on different beamlines. There is a need to develop new multi-modality characterization techniques that can simultaneously show both microstructural and chemical properties to study the relationship between microstructure and electrochemical performance.

Here, we develop innovative *in situ* correlative full field XCS imaging (XCS-I) and XCT. This work has three innovations. Firstly, we have developed a method using XCS to quantify Li stoichiometry of cathode active materials which is usually difficult to achieve because the weak Li signals are often masked by the strong signals from the TM elements in the cathode active materials and in the stainless steel coin cell casings [34,36,37,39,40]. The XCS method is not only sensitive towards Li but also towards other heavy elements because XCS focuses on analyzing the electron momentum density of electrons. Although this method cannot quantify the exact chemical states without calibration, this method can quantitatively compare different chemical states of the elements through comparing the measured electron momentum densities of valence electrons. Secondly, this work expands on the previous pencil beam (or point-by-point) XCS technique by employing a high aspect ratio rectangular cross-section synchrotron X-ray beam and an energy resolving spectroscopic imaging detector, a high-energy X-ray imaging technology (HEXITEC) CdZnTe detector [41]. The HEXITEC detector obtains spatially resolved XCS-I of all voxels across the entire plane of the LIB within a single capture, reducing the scanning duration from ~30 h to 12 min for the same area of interest. Thirdly, we combine XCS-I and XCT to quantify spatially resolved Li^+ chemical stoichiometry distribution in the 3D electrode microstructure inside an LIB with commercially standard battery geometry and packaging within a single experiment. We compare Li^+ ion diffusion and chemical stoichiometry in two types of ultra-thick $LiNi_{0.8}Mn_{0.1}Co_{0.1}O_2$ (NMC811) cathodes, an anisotropic microstructure of vertically oriented pore channels fabricated by the DIT technique and a more isotropic microstructure fabricated by isotropic ice templating (IIT) to show the anisotropic microstructure reduces pore directional tortuosity, increases Li^+ ion diffusion coefficient, increases Li^+ chemical stoichiometry in thick electrodes to improve the energy storage performance at the device level.

2. Materials and methods

2.1. Materials, electrode fabrication and battery assembly

Electrode slurry was prepared by homogeneously mixing NMC811, Super P electrical conductivity enhancer and binder at a weight ratio of 90: 5: 5. A rapid DIT was used to fabricate the electrodes with vertical orientation of pore arrays [21–23]. During the DIT process, a Cu cold finger provided a steep freezing temperature gradient to the electrode slurry. At supercooling, ice crystals were first nucleated in the electrode slurry on the surface of the cold finger. The ice dendrites then grew in parallel to the applied temperature gradient, pushing NMC811 and carbon electrical conductivity enhancer particles into the regions in-between the ice dendrites. Finally, the ice crystals were sublimed during freeze drying, leaving vertically aligned pore arrays. For comparison, another type of electrode was fabricated by IIT where freezing was from all directions using the same electrode slurry. Both types of electrode had a thickness of ~1 mm and a diameter of ~6.5 mm controlled by the mold size during the electrode fabrication, it is possible to further increase the diameter through changing the mold size [21]. The loading density of the electrode materials was 3.1 ± 0.2 g cm^{-3} for both electrodes. Standard CR2032 coin cells (total thickness 3.2 mm), a common tool in battery research, were assembled. Each coin cell contained a stainless steel spacer, a polyethylene separator and a Li metal foil counter electrode, schematic in Fig. S1. Both cathode and separator were soaked with a standard liquid electrolyte containing 1 M $LiPF_6$ in a 1:1 vol% mixture of ethylene carbonate (EC) and dimethyl carbonate (DMC). The cells were galvanostatically charged and discharged using a Gamry Reference 600/EIS300 potentiostat/galvanostat, and the data was recorded every second. The NMC811 particles were examined by scanning electron microscopy (SEM, Merlin Analytical, Zeiss), phase identification was carried out using X-ray diffraction (XRD, D5000, Siemens with Cu_α radiation $\lambda = 1.5$ Å).

2.2. Correlative full field X-ray compton scattering imaging and X-ray computed tomography

The experiment configuration is shown in Fig. 1. We used Si (111) bent Laue monochromator (beamline I12, Diamond Light Source, UK) to provide an X-ray beam with a photon energy of 114.64 keV, measured using a NIST 674 b CeO_2 powder diffraction standard. The XCT detector was positioned behind the LIB sample to collect the transmitted X-rays. The HEXITEC detector was positioned at 90° to the incident X-ray beam, collecting the scattered photons from the top of the LIB cell. The LIB cell was placed in a custom-made holder connected to a potentiostat and mounted on a goniometer, enabling centering and aligning the battery position horizontally with respect to the incident beam and the transmission imaging camera. The battery was charged from an open circuit voltage (OCV) to 4.3 V at a rate of 0.5C (1C indicates ~1 h charge/discharge). The X-ray beam was first set to be 25 mm (horizontal) x 5 mm

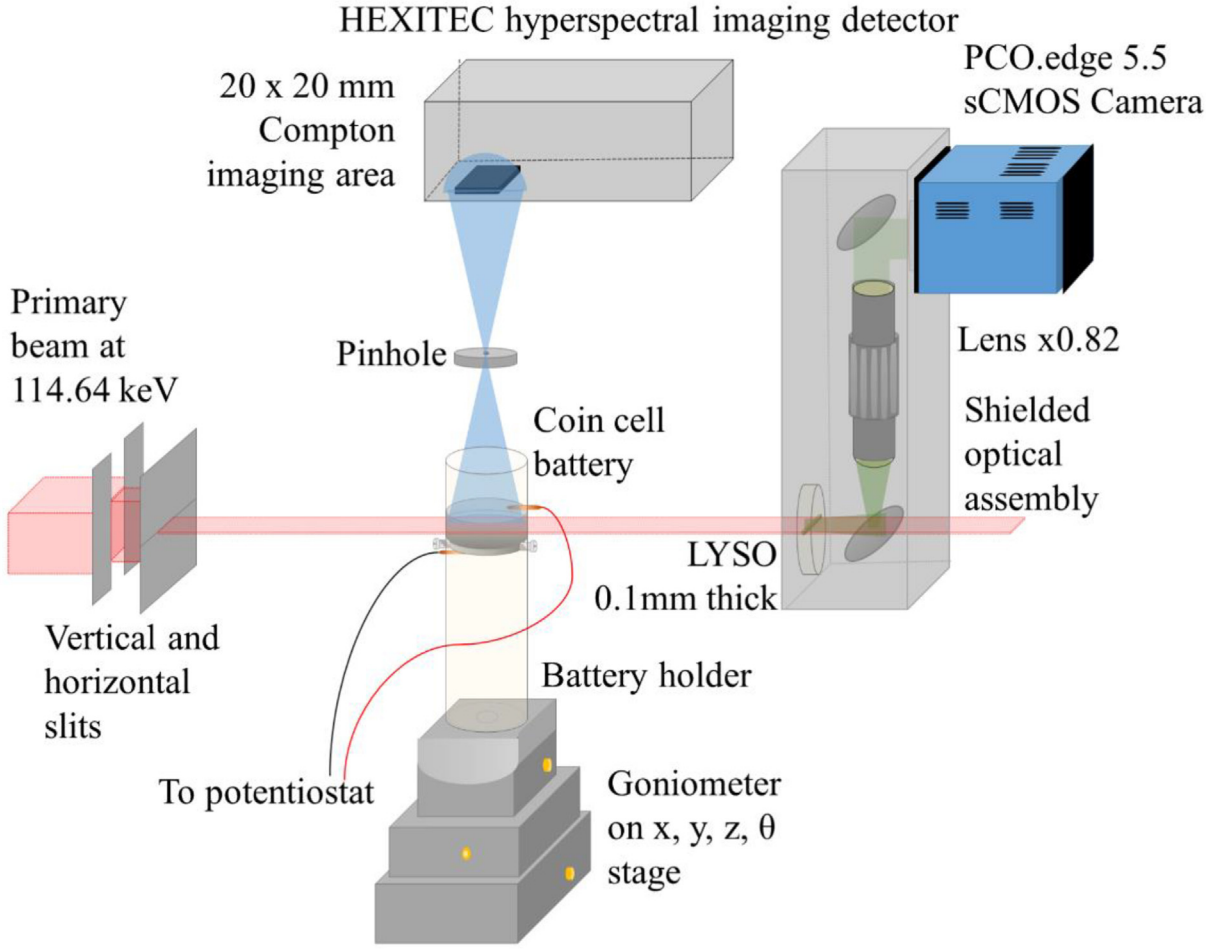

Fig. 1. Schematic of the correlative X-ray Compton scattering imaging (XCS-I) and X-ray computed tomography (XCT) technique experimental set-up.

(vertical) using beam defining slits to cover the entire battery cell and collect XCT images. The X-ray beam of the same energy was then reduced to 25 mm (horizontal) x 0.25 mm (vertical) to capture the XCS signals of all voxels across the entire horizontal plane (*x*-*y*) of the battery in the middle vertical height (*y*-*z*) of the cathode. The LIB was then discharged from 4.3 V to 2.75 V, and a repeat set of XCT and XCS images collected.

2.3. X-ray compton scattering imaging (XCS-I)

The bandwidth of the X-ray beam was set to its maximum value of ~10^{-3} to maximize the incident flux while being narrower than the energy resolution of the HEXITEC detector. If necessary, Cu filters could be used to reduce flux. The temperature of the HEXITEC CdZnTe detector was at 18 °C and the applied bias voltage was −1200 V. The detector had 80 x 80 voxels at a 250 μm voxel pitch, operating at 9 kHz frame rate with the energy and position of every individual X-ray photon extracted from the raw frames of data captured by the application-specific integrated circuit (ASIC), and the resulting data was stored in a data cube of 80 x 80 voxels and 100 energy channels. The raw data from the HEXITEC detector was processed into XCS energy spectra per voxel [42]. The XCS energy spectra images were formed by integrating the counts as a function of energy within the scanning duration voxel-by-voxel. The average energy resolution of a voxel was measured to be 0.79 ± 0.15 keV using the 59.54 keV line from an Am-241 [43]. A pinhole configuration was used to project the Compton scattering image onto the HEXITEC detector. Removable 2 mm thick tungsten disks (Amptek Inc., USA) were used as the pinhole with 200 μm straight through hole. Ignoring transmission through the edge of the pinhole, the 200 μm diameter pinhole had an acceptance angle of 5.7°. The pinhole was placed in an optical mount and a rail system was used to align the HEXITEC detector to the pinhole as a single assembly with the ability to change the distance between the detector and pinhole. This assembly was placed inside a lead shielded box. The battery sample can be raised or lowered to change the pinhole to sample distance. The distance ratio between the HEXITEC detector to pinhole and pinhole to sample was approximately 1:1 in this experimental configuration with a field of view of roughly 20 × 20 mm^2 with 250 μm detector voxels, the spatial resolution can be improved by a factor of two simply by increasing the detector distance [44]. Each XCS-I scan took ~12 min.

The Compton profile was generated from the measured XCS energy spectrum main peak at 94 keV at each voxel through [45]:

$$\frac{p_z}{mc} \cong \frac{E_2 - E_1 + \left(\frac{E_2 E_1}{mc^2}\right)(1 - cos\ \theta)}{\sqrt{E_1^2 + E_2^2 - 2E_1 E_2\ cos\ \theta}} \quad (1)$$

where p_z is a projection of the electron momentum of electrons in both core and valence orbitals of the $Li_xNi_{0.8}Mn_{0.1}Co_{0.1}O_2$ compound, E_1 and E_2 are energies of the incident and Compton scattered X-rays respectively, m is the electron mass, c is the speed of

light and Θ is the scattering angle. The S-parameter was calculated through [37]:

$$S = \frac{S_L}{S_H} \tag{2}$$

where S_L and S_H are the integral of low and high electron momentum densities from the Compton profiles:

$$S_L = \int_{-1}^{1} J(p_z)dp_z \tag{3}$$

$$S_H = \int_{-5}^{-1} J(p_z)dp_z + \int_{1}^{5} J(p_z)dp_z \tag{4}$$

The value of the Li^+ chemical stoichiometry x in $Li_xNi_{0.8}Mn_{0.1}Co_{0.1}O_2$ was quantified through finding the relationship between x and the S-parameter [37]. Firstly, we calculated the theoretical Compton profiles of $Li_xNi_{0.8}Mn_{0.1}Co_{0.1}O_2$ when x = 1, 0.75, 0.5, 0.25 and 0 following the non-relativistic orbital and total-atom Compton profiles $J_{nl}(Q)$ and $J(Q)$ table [46] based on Equation (1). We then calculated the S-parameter of the theoretical Compton profiles of $Li_xNi_{0.8}Mn_{0.1}Co_{0.1}O_2$ at each of the set x values following Equations (2)–(4). We plotted a graph of S-parameter and x in $Li_xNi_{0.8}Mn_{0.1}Co_{0.1}O_2$ for x = 1, 0.75, 0.5, 0.25 and 0. To check consistency between the calculated and experimentally obtained x values, we extracted the $Li_xNi_{0.8}Mn_{0.1}Co_{0.1}O_2$ DIT and IIT cathodes from the discharged batteries, suspended the cathode samples in 1 M HNO_3 at a concentration of 90 mg/ml homogeneously through ultrasonication (15 min) in an ice bath, and performed post-mortem inductively coupled plasma atomic emission spectrometry (ICP-AES, Agilent 5800, accuracy ±0.01 wt%) of the cathode to measure the wt% of Li following the method in Ref. [38].

2.4. X-ray computed tomography (XCT)

The XCT projections were collected using a 0.1 mm thick lutetium yttrium orthosilicate (Lu_2SiO_5: Ce) LYSO single crystal scintillator and then imaged by the scientific CMOS camera (PCO.edge 5.5 sCMOS camera, PCO AG) through a mirror and lens configuration. The imaging camera module 3 from beamline I12: JEEP [47] was used (field of view of 8 mm × 7 mm, pixel size of 3.24 μm). A double field of view measurement technique was used for the XCT measurements with off-centered samples because the sample horizontal size exceeded a single field of view [48]. A total of 3600 radiographic projections were taken with an exposure time of 9 ms per projection. XCT reconstructions were performed using the SAVU pipeline, incorporating the Astra filtered back projection algorithm [49]. 3D image processing, quantification, and data visualization were performed using a combination of MATLAB 2019b, ImageJ, and Avizo 2019.2 [36].

3. Results and discussion

3.1. Physical properties

Fig. 2a is a gray scale reconstructed XCT cross sectional slice in the *y-z* plane showing the locations of the thick cathode, separator, Li counter electrode and spacer inside the coin cell battery. Fig. 2b shows an XCS-I slice in the *x-y* plane of the battery showing the cathode region (labeled in orange). Exemplary images of the reconstructed XCT and full-field XCS-I slices (Fig. S2) demonstrate that XCS-I can sufficiently capture key components of the coin cell battery and can be used to compare with the XCT data.

The XRD pattern of the as-received NMC811 particles (Fig. S3) matches with the crystal structure of NMC811. The SEM image (Fig. S4) shows the particles have 4–16 μm secondary particles containing nanometer scale primary particles. The cathode was virtually extracted from the battery, series of gray scale *y-z* XCT slices (Fig. 3a and b) and the 3D segmented volume (Fig. 3c) of the DIT cathode show the vertically oriented pore arrays through the electrode thickness. The diameter of the pore channel for the DIT cathode was 10–15 μm. In contrast, the gray scale *y-z* XCT slice (Fig. S5) and the 3D segmented volume (Fig. 3d) of the IIT cathode exhibit a porous microstructure with more random pore orientations. The overall estimated pore volume, ϵ, was 23% and 25% for the DIT and IIT cathodes, respectively. Both pore volumes were comparable with that of conventional SC electrodes [8].

The Li^+ ion diffusion flux along the *x-y* and *y-z* planes in the porous network of these two types of cathode was simulated based on the XCT microstructure data using finite difference method [50]. The sub-domain of the electrode microstructure from the XCT data was firstly divided into voxels and an ion concentration gradient was imposed between the opposing faces of the sub-domains. Ions were then simulated to move through the microstructure to approach equilibrium. Fig. 4a shows that the simulated Li^+ ion diffusion flux through the electrode thickness (the kinetically favorable Li^+ ion diffusion direction during charge and discharge [51]) is higher than the flux along the electrode plane for the DIT electrode. Fig. 4b shows the simulated Li^+ ion diffusion flux in the *y* direction along the electrode plane (*x-y*) was higher than the flux through the electrode thickness for the IIT electrode, in agreement with previous studies that show electrodes composed of commercial NMC811 particles with a broad size range (4–16 μm) experience microstructural self-arrangement where the particles manifest a strong preferential horizontal arrangement (parallel to the *x-y* plane) that further restrict Li^+ ion diffusion [52].

The pore tortuosity τ represents the deviations of Li^+ diffusion pathways from the straight cylindrical pores of uniform diameters [53,54]. The tortuosity of a structure plays a vital role in the transport of mass and charge in electrochemical devices and is thus a function of microstructural characteristics [55] where $\tau = 1$ represents an idealized straight pore channel with a uniform diameter; hence, the closer τ towards 1, the straighter the pore geometry. τ was estimated from comparing the Li^+ ion diffusive flux through the measured pore network (F_p) with the Li^+ ion flux through an open volume of the same size (F_{cv}) using [50]:

$$\tau = \frac{F_{CV}}{F_P}\epsilon \tag{5}$$

τ was estimated at 2.1 and 4.5 through the electrode thickness for the DIT and IIT electrodes respectively, showing significantly straighter pore channels for the DIT electrode than the IIT electrode. With similar porosity but much lower electrode thickness (45–66 μm), previous studies have shown pore tortuosity of 3.5–4.8 [52]. The directional Li^+ ion diffusion coefficient $D^{directional}$ in the porous network of the electrodes was quantified by Ref. [50]:

$$D^{directional} = D\frac{\epsilon}{\tau} \tag{6}$$

where D is the concentration-dependent intrinsic Li^+ ion diffusion coefficient of the electrolyte (~10^{-6} cm^2/s for the electrolyte in this experiment [56]). $D_{directional}$ in the porous network along the through-thickness direction was estimated at 1.1 x 10^{-7} and 5.6 x10^{-8} cm^2/s for the DIT and IIT electrodes, respectively. Note that

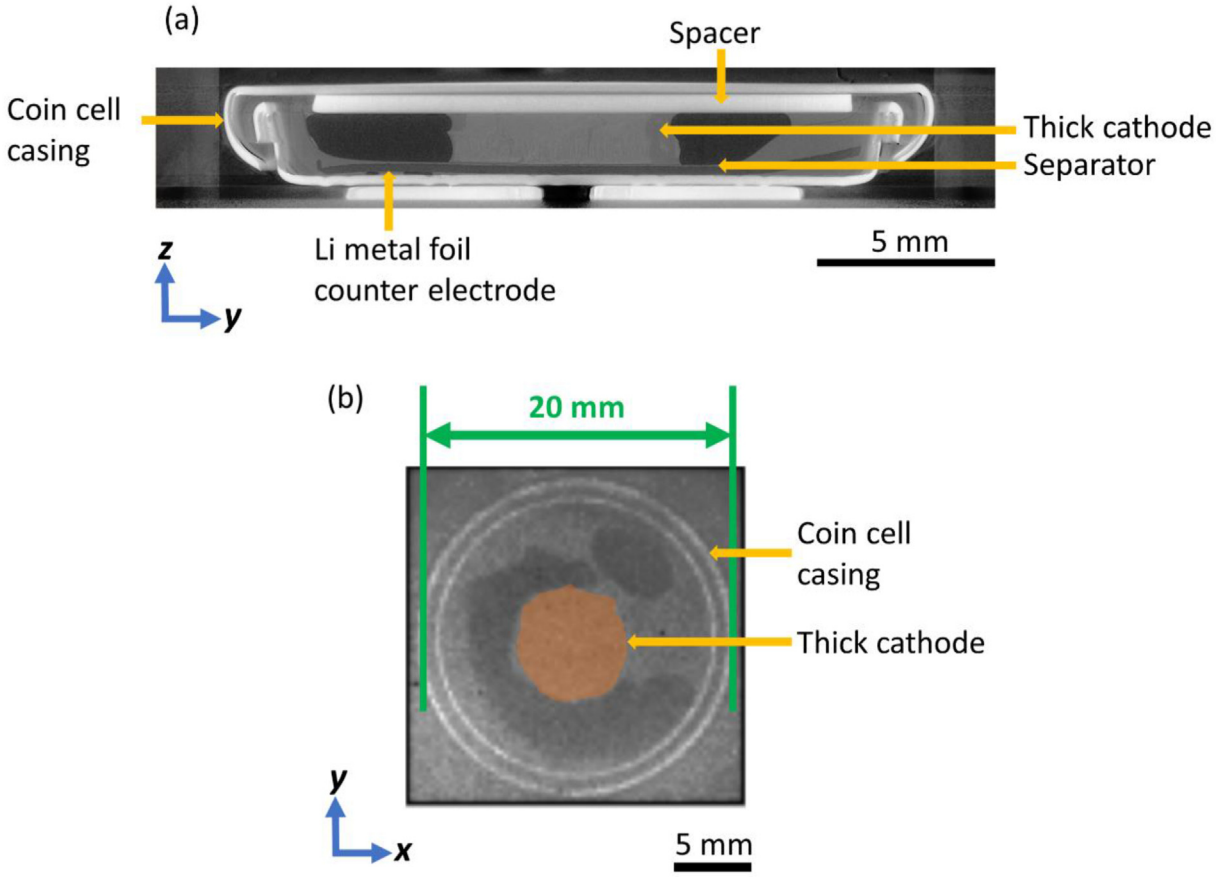

Fig. 2. (a) Reconstructed XCT slice (*y*-*z* plane) of the battery and the components inside the battery; and (b) XCS-I slice (*x*-*y* plane) of the battery where false color is used to show the cathode region.

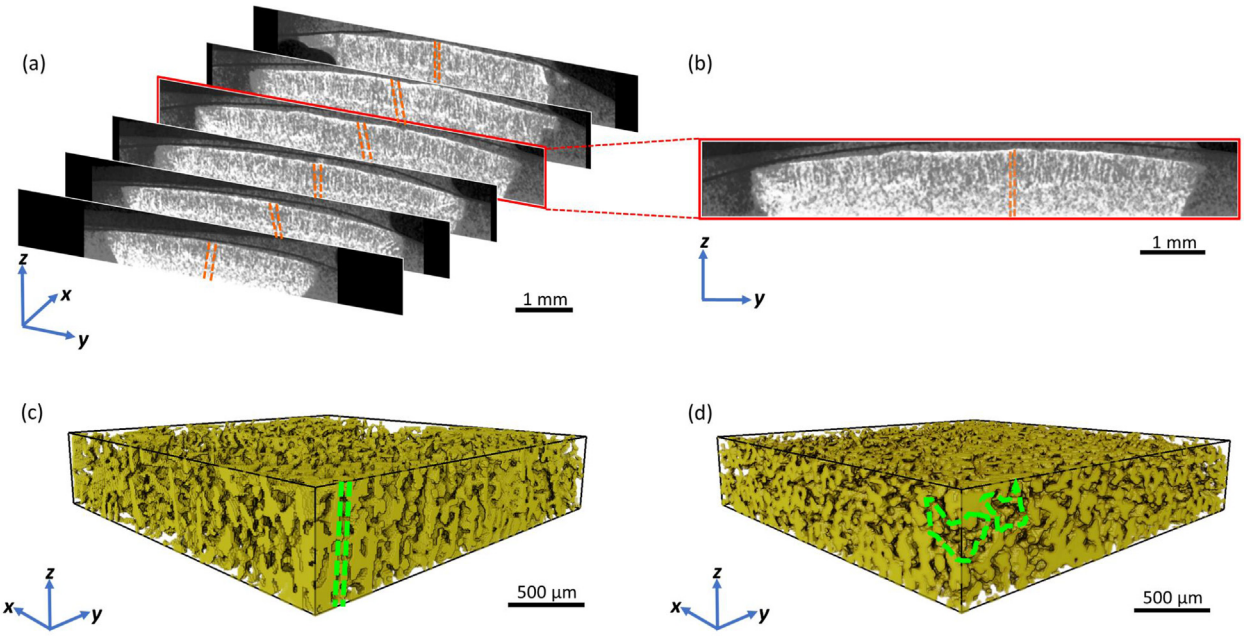

Fig. 3. (a) Gray scale XCT slices and (b) one magnified *y*-*z* slice of the DIT cathode extracted virtually from the battery; 3D volume rendering of a region of interest extracted virtually from the cathodes showing (c) the vertically oriented pore arrays inside the DIT cathode; and (d) the random pore orientations inside the IIT cathode.

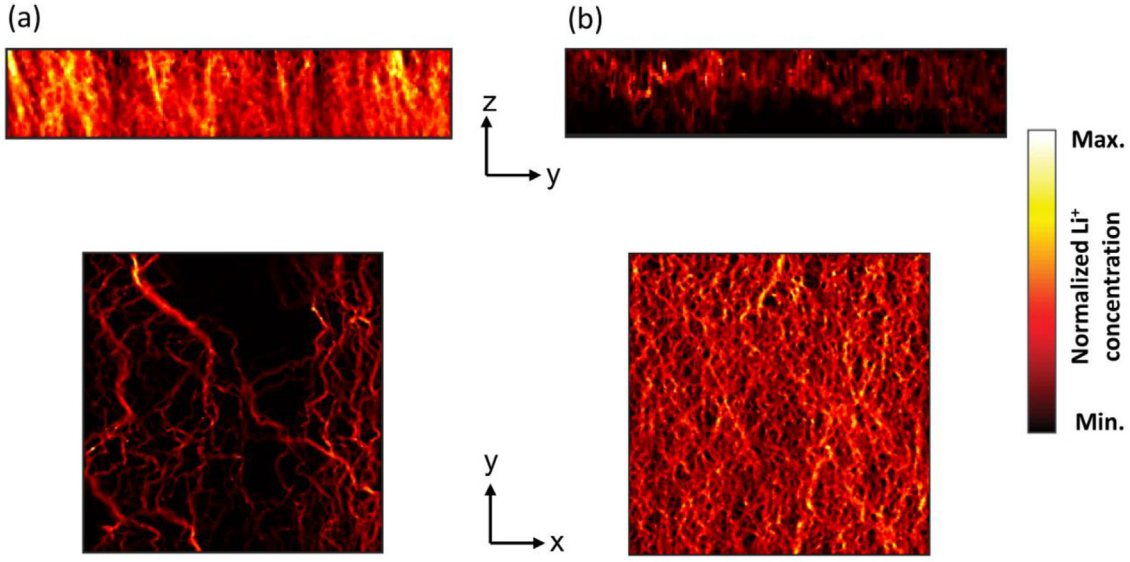

Fig. 4. Simulated Li $^{+}$ ion diffusion flux in the *y*-*z* and *x*-*y* directions for the (a) DIT; and (b) IIT cathodes.

the pore tortuosity τ in the *x* and *y* directions along the *x*-*y* plane is 4.0 and 4.3 respectively for the IIT electrode, and 10.5 and 11.2 respectively for the DIT electrode. Hence, τ in the *x* and *y* directions is similar to each other along the *x*-*y* plane for both electrodes.

3.2. Electrochemical performance

Fig. 5a and S6 show the charge and discharge curves of the DIT and IIT cathodes at increasing C rates. The potential range of 2.75–4.3 V was chosen because previous studies show that the NMC811 lattice parameter *c* and the crystal unit cell volume collapse rapidly above 4.3 V [57]. The DIT cathode exhibited higher reversible capacities at all C rates, e.g. 201 mAh/g (61 mAh cm^{-2} and 603 mAh cm^{-3}) compared with 167 mAh/g (49 mAh/cm^2 and 489 mAh cm^{-3}) for the IIT electrode at 0.1C. For comparison, the gravimetric, areal and volumetric capacities for the conventional ~100 μm thin cathodes of NMC811 are 190–200 mAh/g, 5.5–8 mAh/cm^2 and 522–575 mAh cm^{-3}, respectively at 0.1C [58,59]. Fig. 5b shows the reversible capacity was maintained at 74% from 0.1 to 2C for the DIT cathode, higher than 66% and ~70% for the IIT and conventional SC cathodes [60] respectively at the same C rates. Previous results show that ion diffusion is restricted in the thick (>150 μm) electrodes even at low (dis)charge rates of 0.1C [4,61] which is in agreement with the lower capacity of the thick IIT electrode at the slow C rates. Due to the significant higher electrode thickness, the actual current applied for (dis)charge was 10–20 times higher than the actual current applied to the conventional SC electrodes for rate capability measurements [20]. Previous reports show that at such high current at higher C rates (e.g. 1C, 2C), a large polarization exists at the Li metal anode that restricts the battery performance [20]. Therefore, the capacity difference between the DIT and IIT electrodes at ≥1C did not increase further because the anode became the rate determining factor. Since thick electrodes reduce the proportion of inactive components (e.g. current collectors of Al and Cu foil, separator) within the battery cell-stacks, an LIB containing the thick DIT NMC811 cathode increases the energy density to 319 Wh/kg (839 Wh/L) at 0.1C compared with 279 Wh/kg (726 Wh/L) for the conventional LIBs using the SC cathodes reported previously [36,62], equivalent to an average of 15% increase in the energy density (mathematical workout in SI). The DIT and IIT electrodes were made of exactly the same materials. The only difference was that the DIT electrode was applied directional freezing while the IIT electrode was applied isotropic freezing during the electrode fabrication. Therefore, the difference in their electrochemical performance was due to the difference in their microstructure.

Electrochemical impedance spectroscopy (EIS) was further used to investigate the two types of cathodes. Their corresponding Nyquist plots are shown in Fig. 5c and d. The intercept of the Nyquist curves with the real *Z*-axis at the highest frequency represents the equivalent series resistance (R_s) of the cathode and the electrolyte [63]. R_s is 3.7 and 4.6 Ω cm^2 for the DIT and IIT cathodes, respectively, showing a slight reduction in R_s possibly due to the more electrically connected particles in the aligned pillars of the DIT electrode [19]. The diameter of a best-fit semi-circle by the data in the high-medium frequency represents the charge resistance (R_{CT}) of the cathode [64], R_{CT} is 10.8 and 28.0 Ω cm^2 for the DIT and IIT cathodes, respectively. Both the lower R_{CT} and the higher gradient of the Nyquist tail at low frequency for the DIT cathode confirmed faster Li $^{+}$ ion mobility in the electrode [65], corroborating the lower pore tortuosity τ and the higher directional Li $^{+}$ ion diffusion coefficient $D^{directional}$ calculated from the XCT results and the higher capacity and rate capability from the galvanostatic (dis) charge results. Fig. S7 shows the Coulombic efficiency of both types of cathodes at 0.1C, the initial Coulombic efficiency of the DIT electrode (93%) at the first cycle was higher than the IIT electrode (87%). The Coulombic efficiency of both electrodes became stable and reached ≥99% from the 4th cycle to 100th cycle. The slightly higher initial Coulombic efficiency of the DIT electrode may be due to the more homogenized ion distribution and current through the electrode, leading to reduced overpotential and polarization resistance [66], corroborating the lower impedance of the DIT electrode from the EIS measurements.

3.3. Quantum physical and chemical properties

The binarized XCT cathode volume and XCS-I were superimposed on each other to extract the voxel-by-voxel XCS energy spectra of the cathode only excluding the cell parts. The total absorption cross-section is very small at ≥100 keV [67], and the radiation damage of the cathode material from the incident photons is usually negligible [68] because the majority of the incoming high-energy photon beams (115 keV) penetrate through the

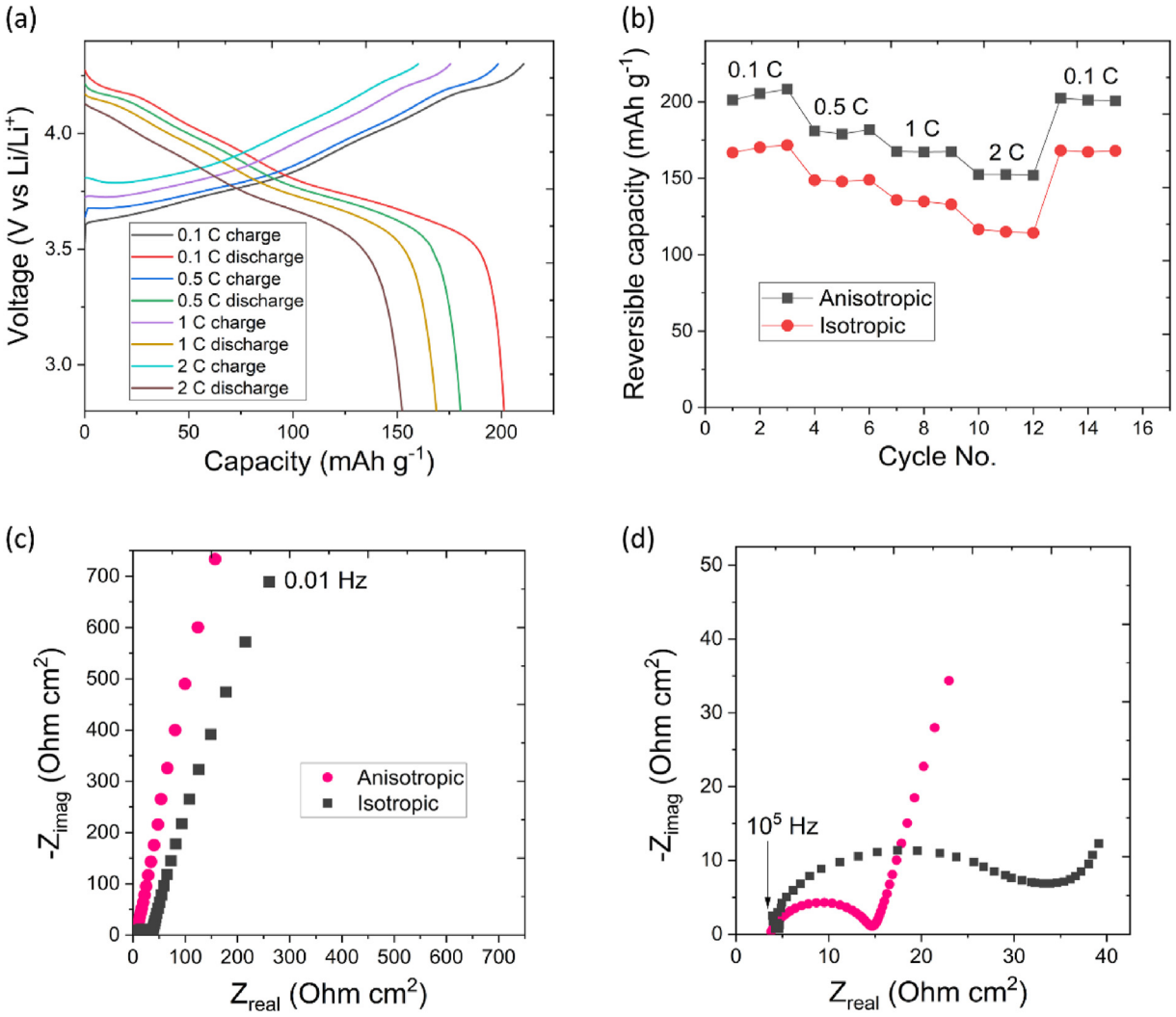

Fig. 5. (a) Charge and discharge curves of the DIT cathode at increasing C rates; (b) rate capability of the DIT and IIT cathodes; (c) EIS Nyquist plot of the two types of cathodes in the full 10^5–0.01 Hz frequency range; and (d) enlarged Nyquist plot in the high frequency range, showing complex impedance of the two types of cathodes in batteries.

cathode material without being absorbed, e.g. the mass absorption coefficients of Ni, Mn and Co was reduced exponentially from 10^4 to 0.1 cm^2/g from 8 keV (Cu Kα laboratory X-ray) to 115 keV [69]. Fig. 6a shows the XCS energy spectra among the lateral voxels in the middle depth region of the DIT cathode in the charged and discharged states. The peak at 94 keV is due to the energy of the incoherently scattered photons with an incoming energy of 115 keV [70]. The other small peaks in the XCS energy spectra are due to the fluorescent K_α and K_β lines for Cd (23 and 26 keV) and Te (27 and 31 keV) from the HEXITEC sensor [71], a mixture of background and fluorescent X-rays (50–70 keV) from the W pinhole and Pb shielding around the HEXITEC detector [71], the low energy threshold of the detector (~5 keV) [72] and a small distinct peak (115 keV) due to X-ray coherent scattering [73]. In comparison, Fig. S8 shows the XCS energy spectra among the lateral voxels in the same region of the IIT cathode in the charged and discharged states. The main peak position at 94 keV remained the same for both types of cathodes, showing the elements present in the cathodes remained the same for both types of fabrication. However, the difference in intensity of the incoherently scattered photons between the charged and discharged states is larger for the DIT cathode than the IIT cathode, indicating the chemical stoichiometry change is larger for the DIT cathode which is quantified below.

The probability of a photon being incoherently scattered by materials mainly depends on the electron density of the materials [74]. Since the electron density of NMC811 is significantly higher than that of conductive carbon, polymeric binder and liquid electrolyte in the pores of the electrode [75], the collected XCS signals are mainly due to NMC811 [34]. The intensity of the peak dN is related to the electron density of the NMC811 active material ρ_e. A Compton profile shows the electron momentum density of a redox orbital [76] and was then generated from the XCS energy spectrum main peak at 94 keV at each voxel. Fig. 6b and Fig. S9 show the Compton profile among the lateral voxels in the middle depth region of the DIT and IIT cathodes respectively in the charged and discharged states. The slow-moving valence electrons exhibit lower kinetic energy (lower electron momentum $-1 < p_z < 1$ in the Compton profile) than the core electrons (higher electron momentum $-5 < p_z < -1$ and $1 < p_z < 5$ in the Compton profile) [37,40]. The larger difference in electron momentum density of the valence electrons between the charged and discharged states for the DIT cathode than the IIT cathode indicates a larger change of Li^+ chemical stoichiometry as the valence electrons are involved in the redox reactions with Li^+ during (dis)charge.

The S-parameter was introduced to indicate the proportion of occupied valence electron orbitals among the core electron orbitals

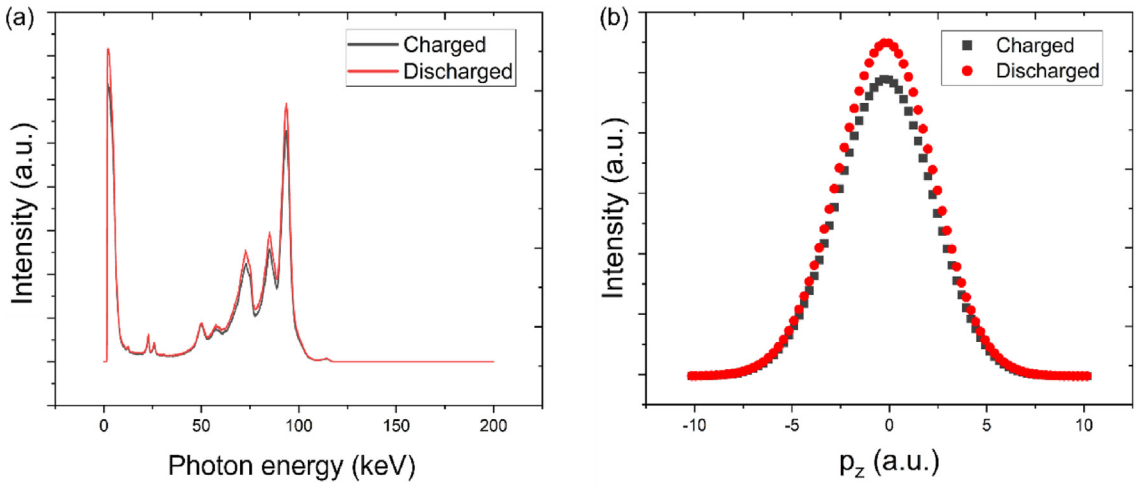

Fig. 6. (a) XCS photon energy spectra; (b) Compton profile of the lateral voxels in the middle depth region of the DIT cathode in the charged and discharged states.

in the $Li_{1-x}Ni_{0.8}Mn_{0.1}Co_{0.1}O_2$ compound [40]. The S parameters were estimated at 0.46 and 0.74 in the middle depth region of the DIT cathode in the charged and discharged states respectively, and 0.48 and 0.53 in the same region of the IIT cathode in the charged and discharged states respectively, these quantification results corroborate the observations of the Compton profiles. We then quantify Li^+ chemical stoichiometry in $Li_xNi_{0.8}Mn_{0.1}Co_{0.1}O_2$ through finding the relationship between the S-parameter and *x*. Briefly, this is quantified through first calculating the theoretical Compton profiles of the core and valence electrons in $Li_xNi_{0.8}Mn_{0.1}Co_{0.1}O_2$ for $x = 1$, 0.75, 0.5, 0.25 and 0 using first-principles Korringa-Kohn-Rostoker coherent-potential-approximation (KKR CPA) within the framework of local spin-density approximation (LSDA) [77] and Mann's numerical relativistic Hartree-Fock wavefunction model [46,78]. The extracted $Li_xNi_{0.8}Mn_{0.1}Co_{0.1}O_2$ cathode from the discharged battery was suspended and then calibrating using our experimental results to take into account the environmental conditions during charge and discharge. Fig. S10 shows the calculated S-parameter varies linearly with the Li^+ chemical stoichiometry *x* in $Li_xNi_{0.8}Mn_{0.1}Co_{0.1}O_2$, so we can quantify the Li^+ chemical stoichiometry x in $Li_xNi_{0.8}Mn_{0.1}Co_{0.1}O_2$ in each voxel from the S-parameter. We map the voxel-by-voxel distribution of the Li^+ chemical stoichiometry in the same middle depth region of the DIT and IIT cathodes in the charged and discharged states inside the working battery (Fig. 7). The ICP-AES results showed 0.48 wt% and 0.36 wt% Li in the prepared suspensions containing the DIT and IIT

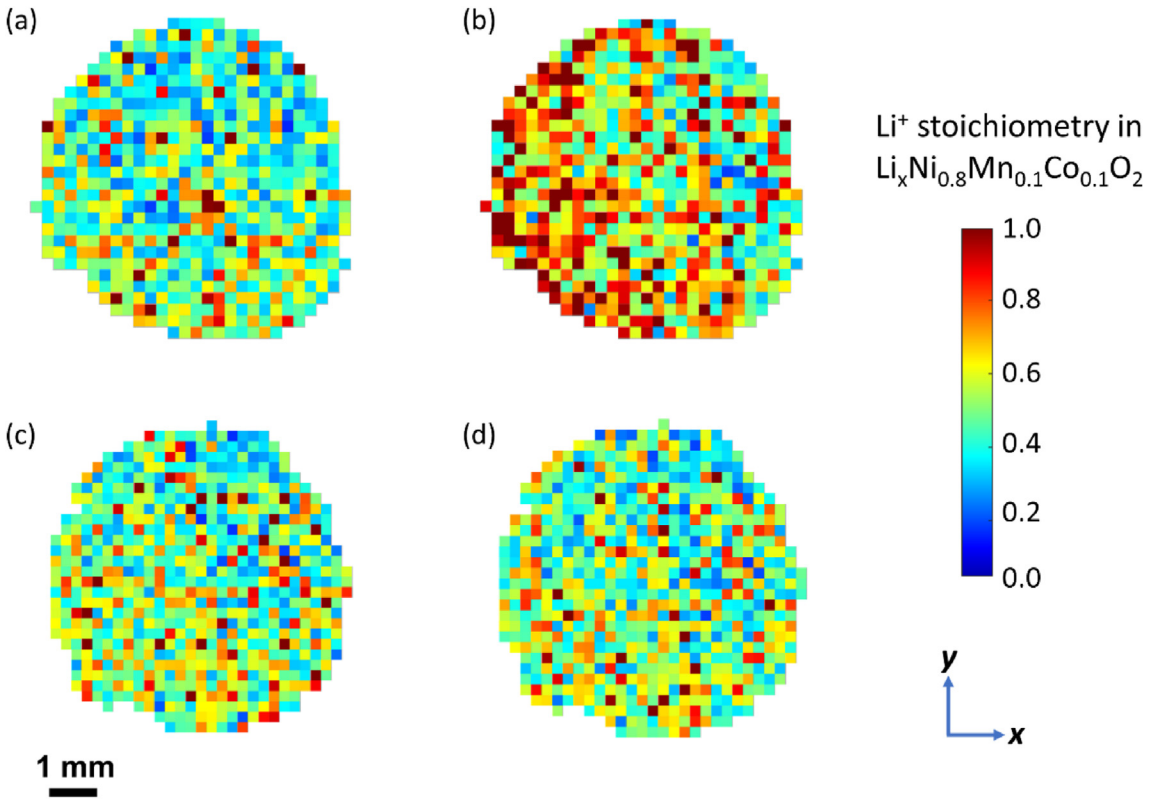

Fig. 7. XCS-I results showing color maps of the lateral distribution of Li^+ chemical stoichiometry voxel-by-voxel in the same middle depth region of the DIT cathode (a) when charged to 4.3 V; (b) when discharged to 2.75 V; and of the IIT cathode (c) when charged to 4.3 V; (d) when discharged to 2.75 V.

cathode samples respectively, reflecting 5.82 wt% and 4.38 wt% of Li content in $Li_xNi_{0.8}Mn_{0.1}Co_{0.1}O_2$ taking into account the concentration of the prepared suspensions using previous reported method in Ref. [38], correlating to x values of 0.8 and 0.6 for the DIT and IIT cathodes respectively. These x values correspond to S-parameters of 0.71 and 0.51 from Fig. S10, in agreement with the measured S-parameters from the XCS results ±4%. Using Beer Lambert law, it is calculated that the X-ray attenuation difference of the electrode region above the region of interest is <1% [79], so it is a fair comparison between the two types of electrodes.

Fig. 7 confirms that the Li^+ stoichiometry is visibly higher in the discharged state than in the charged state for the DIT cathode because Li^+ ions were removed from $Li_xNi_{0.8}Mn_{0.1}Co_{0.1}O_2$ in the charged state and intercalated into $Li_xNi_{0.8}Mn_{0.1}Co_{0.1}O_2$ in the discharged state. The level of inhomogeneity of the lateral distribution of Li stoichiometry across the same electrode plane for both electrodes is surprising, especially the IIT cathode shows a relatively high proportion of the cathode containing low Li stoichiometry in the discharged state, indicating a lower active material utilization for energy storage. The x summarized from the lateral voxels in the middle depth region of the DIT cathode was 0.53 and 0.81 when charged to 4.3 V and discharged to 2.75 V, respectively. The x summarized from all lateral voxels in the middle depth region of the IIT cathode was 0.55 and 0.60 when charged to 4.3 V and discharged to 2.75 V, respectively. The capacities measured from the traditional galvanostatic charge/discharge method in Fig. 5a and b shows the overall capacities of the entire electrodes, whereas the XCS-I results in Fig. 7 show the Li^+ chemical stoichiometry voxel-by-voxel in a specific depth region of the cathodes. The (dis) charge C rate used in the XCS-I experiment (0.5C) was approx. 10 times faster than the rate previously reported to reach ion diffusion equilibrium in NMC811 [57]. The smaller difference in x between 4.3 and 2.75 V for the IIT electrode than the DIT electrode shows significantly restricted ion diffusion in the ultra-thick (1 mm) IIT electrode with tortuous porosity at fast charging.

4. Conclusions

Li concentration in the cathode active materials inside conventional cell configurations has been difficult to image. Our work allows voxel-by-voxel mapping of Li^+ chemical stoichiometry in the electrode microstructure inside a battery using new *in situ* correlative full-field X-ray Compton scattering-imaging (XCS-I) and X-ray computed tomography (XCT). The thick (~1 mm) $LiNi_{0.8}Mn_{0.1}Co_{0.1}O_2$ (NMC811) cathode fabricated by directional ice templating (DIT) exhibited a lower pore tortuosity of 2.1 in the through-electrode-thickness direction than 4.5 for the cathode fabricated by isotropic ice templating (IIT) with the same materials, thickness and porosity (*ca.* 24%). The relating directional Li^+ ion diffusion coefficient was increased from 1.1 x 10^{-7} to 5.6 x10^{-8} cm^2/s in the cathodes. The DIT cathode achieved a high realizable capacity of 201 mAh/g at 0.1C despite its ultra-high thickness and a higher rate capability than the IIT electrode. However, the performance of the IIT electrode was different from the conventional slurry coated electrodes in the literature due to the ultra-high electrode thickness. An LIB containing the thick DIT cathode with a reduced proportion of metallic current collectors has improved Li^+ ion diffusivity and increased energy density by 15% compared with LIBs using conventional thin (50–100 μm) electrodes made by slurry coating (SC). The Li^+ stoichiometry mapping inside the cathode shows heterogeneity in lateral distribution of Li^+. Here, we demonstrate a new correlative imaging capability to corroborate microstructural properties, Li^+ ion diffusion coefficient, energy storage performance and Li^+ chemical stoichiometry mapping of the same electrode within a single experiment.

Credit author statement

C.H., Conceptualization; M.D.W., T.C., S.P.C., O.V.M., M.N.B., K.S., M.C.V., F.V.A., E.L., A.L., C.H., Data curation; C.L.A.L., C.H., M.D.W., M.N.B., F.V.A., Formal analysis; C.H. C.L.A.L., M.D.W., M.N.B., K.S., Funding acquisition; C.H., C.L.A.L., M.D.W., Investigation; C.L.A.L., C.H., Validation; C.L.A.L., C.H., Visualization; C.H., M.D.W., Writing – original draft; C.L.A.L., C.H., T.C., S.P.C., M.N.B., K.S., M.C.V., Writing – review & editing.

Declaration of competing interest

The authors declare that they have no known competing financial interests or personal relationships that could have appeared to influence the work reported in this paper.

Data availability

Data will be made available on request.

Acknowledgments

We are grateful for Prof. Hiroshi Sakurai's advice in this study. This work was carried out with the support of Diamond Light Source, Instrument I12 under proposal MG23400, the EPSRC UKRI Innovation Fellowship (EP/S001239/1, EP/S001239/2), the Faraday Institution projects (FIIF015, FITG34) and the Imperial College London UKRI Impact Acceleration Account (EP/X52556×/1). C.L.A.L. is grateful for the support from the following EPSRC grants (EP/W037483/1, EP/W006774/1, EP/R511638/1, EP/P006566/1, EP/V061798/1, and EP/W003333/1). KS is partially supported by MEXT KAKENHI Grant No. 19K05519, and KS and TC acknowledge support from the UK Royal Society and the Japan Society for the Promotion of Science International Exchange Scheme, award number IEC\R3\193017. The FWO-Flanders and the Ghent University Special Research Fund (BOF-UGent) are acknowledged for the financial support (resp. grant numbers 3G0A0417 W and 01GC1517).

Appendix A. Supplementary data

Supplementary data to this article can be found online at https://doi.org/10.1016/j.mtener.2022.101224.

References

[1] B.A. Simon, A. Gayon-Lombardo, C.A. Pino-Muñoz, C.E. Wood, K.M. Tenny, K.V. Greco, S.J. Cooper, A. Forner-Cuenca, F.R. Brushett, A.R. Kucernak, Combining electrochemical and imaging analyses to understand the effect of electrode microstructure and electrolyte properties on redox flow batteries, Appl. Energy 306 (2022) 117678.
[2] L. Guo, D.B. Thornton, M.A. Koronfel, I.E. Stephens, M.P. Ryan, Degradation in lithium ion battery current collectors, J. Phys.: Energy 3 (2021), 032015.
[3] R.F. Service, Lithium-ion battery development takes Nobel, American Association for the Advancement of Science 366 (2019) 6463, 292.
[4] A.M. Boyce, D.J. Cumming, C. Huang, S.P. Zankowski, P.S. Grant, D.J. Brett, P.R. Shearing, Design of scalable, next-generation thick electrodes: opportunities and challenges, ACS Nano 15 (2021) 18624–18632.
[5] K. Liu, Y. Liu, D. Lin, A. Pei, Y. Cui, Materials for lithium-ion battery safety, Sci. Adv. 4 (2018) eaas9820.
[6] M. Gu, W.-J. Song, J. Hong, S.Y. Kim, T.J. Shin, N.A. Kotov, S. Park, B.-S. Kim, Stretchable batteries with gradient multilayer conductors, Sci. Adv. 5 (2019) eaaw1879.
[7] K. Liu, W. Liu, Y. Qiu, B. Kong, Y. Sun, Z. Chen, D. Zhuo, D. Lin, Y. Cui, Electrospun core-shell microfiber separator with thermal-triggered flame-retardant properties for lithium-ion batteries, Sci. Adv. 3 (2017) e1601978.
[8] X. Lu, A. Bertei, D.P. Finegan, C. Tan, S.R. Daemi, J.S. Weaving, K.B. O'Regan, T.M. Heenan, G. Hinds, E. Kendrick, 3D microstructure design of lithium-ion battery electrodes assisted by X-ray nano-computed tomography and modelling, Nat. Commun. 11 (2020) 1–13.

[9] B. Zhu, G. Liu, G. Lv, Y. Mu, Y. Zhao, Y. Wang, X. Li, P. Yao, Y. Deng, Y. Cui, Minimized lithium trapping by isovalent isomorphism for high initial Coulombic efficiency of silicon anodes, Sci. Adv. 5 (2019) eaax0651.
[10] H. Zhang, H. Ning, J. Busbee, Z. Shen, C. Kiggins, Y. Hua, J. Eaves, J. Davis III, T. Shi, Y.-T. Shao, Electroplating lithium transition metal oxides, Sci. Adv. 3 (2017) e1602427.
[11] B. Shen, S. Wang, W. Tenhaeff, Ultrathin conformal polycyclosiloxane films to improve silicon cycling stability, Sci. Adv. 5 (2019) eaaw4856.
[12] T.W. Verhallen, S. Lv, M. Wagemaker, Operando neutron depth profiling to determine the spatial distribution of Li in Li-ion Batteries, Front. Energy Res. 6 (2018) 62.
[13] O.H. Kwon, J.H. Oh, B. Gu, M.S. Jo, S.H. Oh, Y.C. Kang, J.K. Kim, S.M. Jeong, J.S. Cho, Porous SnO2/C nanofiber anodes and LiFePO4/C nanofiber cathodes with a wrinkle structure for stretchable lithium polymer batteries with high electrochemical performance, Adv. Sci. 7 (2020) 2001358.
[14] K.G. Gallagher, S.E. Trask, C. Bauer, T. Woehrle, S.F. Lux, M. Tschech, P. Lamp, B.J. Polzin, S. Ha, B. Long, Optimizing areal capacities through understanding the limitations of lithium-ion electrodes, J. Electrochem. Soc. 163 (2015) A138.
[15] M. Doyle, J. Newman, Analysis of capacity–rate data for lithium batteries using simplified models of the discharge process, J. Appl. Electrochem. 27 (1997) 846–856, 846–856.
[16] D.-W. Chung, M. Ebner, D.R. Ely, V. Wood, R.E. García, Validity of the Bruggeman relation for porous electrodes, Model. Simulat. Mater. Sci. Eng. 21 (2013), 074009.
[17] X. Wu, B. Song, P.H. Chien, S.M. Everett, K. Zhao, J. Liu, Z. Du, Structural evolution and transition dynamics in lithium ion battery under fast charging: an operando neutron diffraction investigation, Adv. Sci. (2021) 2102318.
[18] C.J. Bae, C.K. Erdonmez, J.W. Halloran, Y.M. Chiang, Design of battery electrodes with dual-scale porosity to minimize tortuosity and maximize performance, Adv. Mater. 25 (2013) 1254–1258.
[19] J.S. Sander, R.M. Erb, L. Li, A. Gurijala, Y.M. Chiang, High-performance battery electrodes via magnetic templating, Nat. Energy 1 (2016) 1–7.
[20] L.-L. Lu, Y.-Y. Lu, Z.-J. Xiao, T.-W. Zhang, F. Zhou, T. Ma, Y. Ni, H.-B. Yao, S.-H. Yu, Y. Cui, Wood-inspired high-performance ultrathick bulk battery electrodes, Adv. Mater. (2018) 1706745.
[21] Huang, C.; Leung, C. L. A.; Leung, P.; Grant, P. S. A solid-state battery cathode with a polymer composite electrolyte and low tortuosity microstructure by directional freezing and polymerization. Adv. Energy Mater., 2002387.
[22] C. Huang, M. Dontigny, K. Zaghib, P.S. Grant, Low-tortuosity and graded lithium ion battery cathodes by ice templating, J. Mater. Chem. 7 (2019) 21421–21431.
[23] C. Huang, P.S. Grant, Coral-like directional porosity lithium ion battery cathodes by ice templating, J. Mater. Chem. 6 (2018) 14689–14699.
[24] R.F. Ziesche, T. Arlt, D.P. Finegan, T.M. Heenan, A. Tengattini, D. Baum, N. Kardjilov, H. Markötter, I. Manke, W. Kockelmann, 4D imaging of lithium-batteries using correlative neutron and X-ray tomography with a virtual unrolling technique, Nat. Commun. 11 (2020) 1–11.
[25] F. Friedrich, B. Strehle, A.T. Freiberg, K. Kleiner, S.J. Day, C. Erk, M. Piana, H.A. Gasteiger, Capacity fading mechanisms of NCM-811 cathodes in lithium-ion batteries studied by X-ray diffraction and other diagnostics, J. Electrochem. Soc. 166 (2019) A3760.
[26] X. Wang, S. Tan, X.-Q. Yang, E. Hu, Pair distribution function analysis: fundamentals and application to battery materials, Chin. Phys. B 29 (2020), 028802.
[27] J. McBreen, M. Balasubramanian, Rechargeable lithium-ion battery cathodes: in-situ xas, J. Occup. Med. 54 (2002) 25–28.
[28] S. Spence, W.-K. Lee, F. Lin, X. Xiao, Transmission X-ray microscopy and its applications in battery material research–A short review, Nanotechnology 32 (2021) 442003, 1–10.
[29] U. Bergmann, P. Glatzel, S.P. Cramer, Bulk-sensitive XAS characterization of light elements: from X-ray Raman scattering to X-ray Raman spectroscopy, Microchem. J. 71 (2002) 221–230.
[30] G. Larraz, A. Orera, J. Sanz, I. Sobrados, V. Diez-Gómez, M. Sanjuán, NMR study of Li distribution in Li 7− x H x La 3 Zr 2 O 12 garnets, J. Mater. Chem. 3 (2015) 5683–5691.
[31] M.A. Hope, B.L. Rinkel, A.B. Gunnarsdóttir, K. Märker, S. Menkin, S. Paul, I.V. Sergeyev, C.P. Grey, Selective NMR observation of the SEI–metal interface by dynamic nuclear polarisation from lithium metal, Nat. Commun. 11 (2020) 1–8.
[32] Y.-C. Hsieh, M. Leißing, S. Nowak, B.-J. Hwang, M. Winter, G. Brunklaus, Quantification of dead lithium via in situ nuclear magnetic resonance spectroscopy, Cell Reports Physical Science 1 (2020) 100139.
[33] J. Liu, Z. Du, X. Wang, S. Tan, X. Wu, L. Geng, B. Song, P.-H. Chien, S.M. Everett, E. Hu, Anionic redox induced anomalous structural transition in Ni-rich cathodes, Energy Environ. Sci. 14 (2021) 6441–6454.
[34] K. Suzuki, A. Suzuki, T. Ishikawa, M. Itou, H. Yamashige, Y. Orikasa, Y. Uchimoto, Y. Sakurai, H. Sakurai, In operando quantitation of Li concentration for a commercial Li-ion rechargeable battery using high-energy X-ray Compton scattering, J. Synchrotron Radiat. 24 (2017) 1006–1011.
[35] H. Hafiz, K. Suzuki, B. Barbiellini, Y. Orikasa, V. Callewaert, S. Kaprzyk, M. Itou, K. Yamamoto, R. Yamada, Y. Uchimoto, Visualizing redox orbitals and their potentials in advanced lithium-ion battery materials using high-resolution x-ray Compton scattering, Sci. Adv. 3 (2017) e1700971.
[36] Huang, C.; Wilson, M. D.; Suzuki, K.; Liotti, E.; Connolley, T.; Magdysyuk, O. V.; Collins, S.; Van Assche, F.; Boone, M. N.; Veale, M. C. 3D correlative imaging of lithium ion concentration in a vertically oriented electrode microstructure with a density gradient. Adv. Sci., 2105723.
[37] K. Suzuki, R. Kanai, N. Tsuji, H. Yamashige, Y. Orikasa, Y. Uchimoto, Y. Sakurai, H. Sakurai, Dependency of the charge–discharge rate on lithium reaction distributions for a commercial lithium coin cell visualized by compton scattering imaging, Condensed Matter 3 (2018) 27, 1–8.
[38] K. Suzuki, A.-P. Honkanen, N. Tsuji, K. Jalkanen, J. Koskinen, H. Morimoto, D. Hiramoto, A. Terasaka, H. Hafiz, Y. Sakurai, High-energy X-ray compton scattering imaging of 18650-type lithium-ion battery cell, Condensed Matter 4 (2019) 66.
[39] K. Suzuki, B. Barbiellini, Y. Orikasa, N. Go, H. Sakurai, S. Kaprzyk, M. Itou, K. Yamamoto, Y. Uchimoto, Y.J. Wang, Extracting the redox orbitals in Li battery materials with high-resolution x-ray compton scattering spectroscopy, Phys. Rev. Lett. 114 (2015), 087401.
[40] K. Suzuki, B. Barbiellini, Y. Orikasa, S. Kaprzyk, M. Itou, K. Yamamoto, Y.J. Wang, H. Hafiz, Y. Uchimoto, A. Bansil, Non-destructive measurement of in-operando lithium concentration in batteries via x-ray Compton scattering, J. Appl. Phys. 119 (2016), 025103.
[41] M. Veale, P. Seller, M. Wilson, E. Liotti, HEXITEC: a high-energy X-ray spectroscopic imaging detector for synchrotron applications, Synchrotron Radiat. News 31 (2018) 28–32.
[42] F. Van Assche, S. Vanheule, L. Van Hoorebeke, M.N. Boone, The spectral x-ray imaging data acquisition (spexidaq) framework, Sensors 21 (2021) 563.
[43] M.C. Veale, P. Booker, S. Cross, M.D. Hart, L. Jowitt, J. Lipp, A. Schneider, P. Seller, R.M. Wheater, M.D. Wilson, Characterization of the uniformity of high-flux CdZnTe material, Sensors 20 (2020) 2747.
[44] E. Liotti, A. Lui, T. Connolley, I. Dolbnya, K. Sawhney, A. Malandain, M. Wilson, M. Veale, P. Seller, P. Grant, Mapping of multi-elements during melting and solidification using synchrotron X-rays and pixel-based spectroscopy, Sci. Rep. 5 (2015) 1–6.
[45] M.J. Cooper, P.E. M, N. Shiotani, N. Sakai, A. Bansil, X-Ray Compton Scattering, Oxford University Press, Oxford, 2004.
[46] F. Biggs, L. Mendelsohn, J. Mann, Hartree-Fock Compton profiles for the elements, Atomic Data Nucl. Data Tables 16 (1975) 201–309.
[47] M. Drakopoulos, T. Connolley, C. Reinhard, R. Atwood, O. Magdysyuk, N. Vo, M. Hart, L. Connor, B. Humphreys, G. Howell, I12: the joint engineering, environment and processing (JEEP) beamline at diamond light source, J. Synchrotron Radiat. 22 (2015) 828–838.
[48] N.T. Vo, R.C. Atwood, M. Drakopoulos, T. Connolley, Data processing methods and data acquisition for samples larger than the field of view in parallel-beam tomography, Opt Express 29 (2021) 17849–17874.
[49] R.C. Atwood, A.J. Bodey, S.W. Price, M. Basham, M. Drakopoulos, A high-throughput system for high-quality tomographic reconstruction of large datasets at Diamond Light Source, Phil. Trans. Math. Phys. Eng. Sci. 373 (2015) 20140398.
[50] S.J. Cooper, A. Bertei, P.R. Shearing, J.A. Kilner, N.P. Brandon, TauFactor: an open-source application for calculating tortuosity factors from tomographic data, Software X 5 (2016) 203–210.
[51] R. Morasch, J. Landesfeind, B. Suthar, H.A. Gasteiger, Detection of binder gradients using impedance spectroscopy and their influence on the tortuosity of Li-ion battery graphite electrodes, J. Electrochem. Soc. 165 (2018) A3459.
[52] X. Lu, S.R. Daemi, A. Bertei, M.D. Kok, K.B. O'Regan, L. Rasha, J. Park, G. Hinds, E. Kendrick, D.J. Brett, Microstructural evolution of battery electrodes during calendering, Joule 4 (2020) 2746–2768.
[53] U. Tröltzsch, O. Kanoun, Generalization of transmission line models for deriving the impedance of diffusion and porous media, Electrochim. Acta 75 (2012) 347–356.
[54] T.-T. Nguyen, A. Demortière, B. Fleutot, B. Delobel, C. Delacourt, S.J. Cooper, The electrode tortuosity factor: why the conventional tortuosity factor is not well suited for quantifying transport in porous Li-ion battery electrodes and what to use instead, npj Computational Materials 6 (2020) 1–12.
[55] B. Tjaden, D.J. Brett, P.R. Shearing, Tortuosity in electrochemical devices: a review of calculation approaches, Int. Mater. Rev. 63 (2018) 47–67.
[56] S.G. Stewart, J. Newman, The use of UV/vis absorption to measure diffusion coefficients in LiPF6 electrolytic solutions, J. Electrochem. Soc. 155 (2007) F13.
[57] K. Märker, P.J. Reeves, C. Xu, K.J. Griffith, C.P. Grey, Evolution of structure and lithium dynamics in LiNi0. 8Mn0. 1Co0. 1O2 (NMC811) cathodes during electrochemical cycling, Chem. Mater. 31 (2019) 2545–2554.
[58] T.M. Heenan, C. Tan, J. Hack, D.J. Brett, P.R. Shearing, Developments in X-ray tomography characterization for electrochemical devices, Mater. Today 31 (2019) 69–85.
[59] D.L. Wood III, M. Wood, J. Li, Z. Du, R.E. Ruther, K.A. Hays, N. Muralidharan, L. Geng, C. Mao, I. Belharouak, Perspectives on the relationship between materials chemistry and roll-to-roll electrode manufacturing for high-energy lithium-ion batteries, Energy Storage Mater. 29 (2020) 254–265.
[60] C. Mao, R.E. Ruther, J. Li, Z. Du, I. Belharouak, Identifying the limiting electrode in lithium ion batteries for extreme fast charging, Electrochem. Commun. 97 (2018) 37–41.
[61] S. Golmon, K. Maute, M.L. Dunn, Multiscale design optimization of lithium ion batteries using adjoint sensitivity analysis, Int. J. Numer. Methods Eng. 92 (2012) 475–494.
[62] C. Huang, P.S. Grant, One-step spray processing of high power all-solid-state supercapacitors, Sci. Rep. 3 (2013) 2393, https://doi.org/10.1038/srep02393.

[63] J. Ou, G. Li, Z. Chen, Improved composite solid electrolyte through ionic liquid-assisted polymer phase for solid-state lithium ion batteries, J. Electrochem. Soc. 166 (2019) A1785.
[64] Y. Su, G. Chen, L. Chen, Y. Lu, Q. Zhang, Z. Lv, C. Li, L. Li, N. Liu, G. Tan, High-rate structure-gradient Ni-rich cathode material for lithium-ion batteries, ACS Appl. Mater. Interfaces 11 (2019) 36697−36704.
[65] N. Schweikert, R. Heinzmann, A. Eichhöfer, H. Hahn, S. Indris, Electrochemical impedance spectroscopy of Li$_4$Ti$_5$O$_12$ and LiCoO$_2$ based half-cells and Li$_4$Ti$_5$O$_12$/LiCoO$_2$ cells: internal interfaces and influence of state-of-charge and cycle number, Solid State Ionics 226 (2012) 15−23.
[66] R. Drummond, C. Cheng, P. Grant, S. Duncan, Modelling the impedance response of graded LiFePO4 cathodes for Li-ion batteries, J. Electrochem. Soc. 169 (2022), 010528.
[67] I. Kaplan, B. Barbiellini, A. Bansil, Compton scattering beyond the impulse approximation, Phys. Rev. B 68 (2003) 235104.
[68] H. Hafiz, K. Suzuki, B. Barbiellini, N. Tsuji, N. Yabuuchi, K. Yamamoto, Y. Orikasa, Y. Uchimoto, Y. Sakurai, H. Sakurai, Tomographic reconstruction of oxygen orbitals in lithium-rich battery materials, Nature 594 (2021) 213−216.
[69] G. Aquilanti, M. Giorgetti, R. Dominko, L. Stievano, I. Arčon, N. Novello, L. Olivi, Operando characterization of batteries using x-ray absorption spectroscopy: advances at the beamline XAFS at synchrotron Elettra, J. Phys. Appl. Phys. 50 (2017), 074001.
[70] Masschaele, B.; Dierick, M.; Van Loo, D.; Boone, M. N.; Brabant, L.; Pauwels, E.; Cnudde, V.; Van Hoorebeke, L. In Tilte2013; IOP Publishing.
[71] A.C. Thompson, D. Vaughan, X-Ray Data Booklet; Lawrence Berkeley National Laboratory, vol. 8, University of California Berkeley, CA, 2001.
[72] P. Kane, Inelastic scattering of X-rays and gamma rays, Radiat. Phys. Chem. 75 (2006) 2195−2205.
[73] R.F. Pettifer, S.P. Collins, D. Laundy, Quadrupole transitions revealed by Borrmann spectroscopy, Nature 454 (2008) 196−199.
[74] F. Balogun, N. Spyrou, Compton scattering tomography in the study of a dense inclusion in a lighter matrix, Nucl. Instrum. Methods Phys. Res. Sect. B Beam Interact. Mater. Atoms 83 (1993) 533−538.
[75] D. Iermakova, R. Dugas, M. Palacín, A. Ponrouch, On the comparative stability of Li and Na metal anode interfaces in conventional alkyl carbonate electrolytes, J. Electrochem. Soc. 162 (2015) A7060.
[76] Y. Sakurai, M. Itou, B. Barbiellini, P. Mijnarends, R. Markiewicz, S. Kaprzyk, J.-M. Gillet, S. Wakimoto, M. Fujita, S. Basak, Imaging doped holes in a cuprate superconductor with high-resolution compton scattering, Science 332 (2011) 698−702.
[77] S. Kaprzyk, A. Bansil, Green's function and a generalized Lloyd formula for the density of states in disordered muffin-tin alloys, Phys. Rev. B 42 (1990) 7358.
[78] A. Bansil, B. Barbiellini, S. Kaprzyk, P. Mijnarends, Electron momentum density and Compton profile in disordered alloys, J. Phys. Chem. Solid. 62 (2001) 2191−2197.
[79] R.W. Ricci, M. Ditzler, L.P. Nestor, Discovering the beer-lambert law, J Chem. Educ. 71 (1994) 983.